AGU
ADVANCING EARTH AND SPACE SCIENCE

JGR Solid Earth

Key Points:

- We studied the effect of scCO$_2$ on fracture permeability evolution and fracture surface characteristics in shales
- Carbonate dissolution and inelastic compaction appear to mitigate each other's impact in controlling permeability
- Time-dependency of the carbonate dissolution and fracture surface degradation process was confirmed in carbonate-rich samples

Supporting Information:

Supporting Information may be found in the online version of this article.

Correspondence to:

S. Hashemi,
shashemi@stanford.edu

Permeability Evolution of Fractures in Shale in the Presence of Supercritical CO$_2$

Sam S. Hashemi[1] and **Mark D. Zoback[1]**

[1]Department of Geophysics, Stanford University, Stanford, CA, USA

Abstract We experimentally examined the impact of supercritical carbon dioxide (scCO$_2$) on fracture permeability and fracture surface characteristics in shales of various compositions. We measured permeability and fracture normal displacement at different effective stresses using both argon and scCO$_2$ as pore fluids. Both natural fractures and saw cuts in intact samples were used in our study. The permeability and fracture normal displacement decrease after multiple loading/unloading cycles, apparently as the result of inelastic compaction. In samples with high carbonate content, we observe an increase in permeability and fracture surface degradation after more than 3.5 days of exposure to scCO$_2$, apparently due to carbonate dissolution. We demonstrate that the sensitivity of permeability to effective normal stress correlates well with the fracture normal displacement. The dependence of permeability on effective normal stress increases after exposure to scCO$_2$ as the fracture surface became more compliant.

Plain Language Summary In this study, laboratory experiments were used to investigate the effect of supercritical carbon dioxide (scCO$_2$) on the fracture permeability and fracture surface characteristics of shales. Supercritical state is characterized by the inability to distinguish whether CO$_2$ is a liquid or a gas. For samples with a wide range of compositions, we measured permeability and fracture normal displacement at different stresses using both argon and scCO$_2$ as pore fluids. Both natural fractures and saw cuts in intact samples were used. The fracture normal displacement and permeability decrease after multiple loading/unloading cycles, apparently as the result of irreversible compaction. In samples with high carbonate contents, we observe an increase in permeability and fracture surface degradation after more than 3.5 days of exposure to scCO$_2$, apparently due to carbonate dissolution. We demonstrate that the sensitivity of permeability to net pressure normal to the fracture surface correlates well with the fracture normal displacement. The sensitivity of permeability on net pressure normal to the fracture surface increases after exposure to scCO$_2$ as the fracture surface became more compliant.

1. Introduction

Supercritical CO$_2$ (scCO$_2$) has been proposed as an alternative fracturing fluid for hydraulic fracturing operations in unconventional reservoirs (Ishida et al., 2012; B. Jia et al., 2019; Pei et al., 2015; Zhang et al., 2017). Under typical reservoir condition, CO$_2$ behaves as a supercritical fluid and adopt properties somewhere between a gas and a liquid above the critical temperature and critical pressure of 31.1°C and 7.37 MPa, respectively. It is argued that the use of scCO$_2$ could result in a more complicated fracture network compared to aqueous-based fluids (Ishida et al., 2012; Li et al., 2016; Zhang et al., 2017), improve shale gas recovery by preferential adsorption behaviors of CO$_2$ over methane, reduce flow blockages and reduce the water consumption (Middleton et al., 2015; Pei et al., 2015; Zhou et al., 2020). For instance, a study by Li and Kang (2018) showed that after scCO$_2$ fracturing, the CO$_2$-retention rate was 39.5% and the shale gas production rate increased 1.5 times. However, it should be noted that the low viscosity of scCO$_2$ reduces its efficiency of carrying proppants into the hydraulic fractures.

In general, shales are fine-grained clastic sedimentary rocks that comprise a mix of clays and very fine-grained fragments of other minerals especially carbonates, quartz, feldspars, pyrite (QFP) and organic matter (Reinsalu & Aarna, 2015). Shale rocks typically have a very low matrix permeability ranging from 10^{-21} to 10^{-18} m^2 (Heller et al., 2014; Kamali et al., 2021). However, the faults and natural fractures are major discontinuities and may result in preferential paths for CO$_2$ leakage. The majority of high-permeability pathways of fluid flow in such low permeability rocks are through faults and fractures (Zoback & Kohli, 2019). One of the important factors influencing the fluid flow of rock fracture and deformation properties is the

hydraulic fracture aperture. When fracture apertures are very small, wall roughness and tortuosity can affect fluid flow. The aperture is affected by the effective normal stress at the fracture surface and by shear displacement that determines the fit of the opposing rough surfaces (Fanchi, 2005). The modified cubic law with parallel plate approximation is generally used to estimate the aperture for fractures (Faoro et al., 2016). Of course, the flow path in natural fractures is tortuous and the fracture surface is not perfectly planar and that the fluid-fracture surface interaction is not uniform; thus, the aperture will be variable and possibly dominated by a few flow channels (Jaeger et al., 2009).

Fully characterizing permeability is difficult under reservoir conditions. Laboratory experiments, however, allow us to specify and control conditions and are a useful method to obtain such knowledge. Y. Jia et al. (2018) showed that $scCO_2$ induced dissolution of carbonates in fractured shale results in permeability increase and fracture opening. In a different experiment where the normal effective stress was applied to the fracture, Yasuhara et al. (2011) indicated that aperture change is likely due to a combination of mechanical crushing and chemical dissolution of contacting asperities. Maneth Wanniarachchi et al. (2017) conducted permeability tests using $scCO_2$ on intact and fractured shale samples under various confining pressures to determine the flow characteristic variations upon fracturing of the reservoir. Also, exposure to $scCO_2$ caused the mechanical weakening of the shale matrix. The uniaxial compressive strength and Young's modulus (E) were reduced after shale-$scCO_2$ interaction (Lu et al., 2019). It is well-known that gas adsorption on clay and organic matter, carbonate dissolution and mechanical deformation during production or CO_2 injection in shales are time-dependent processes. Zhou et al. (2019) investigated the effects of the effective stress, pore pressure, gas adsorption, and stress path on the permeability of fractured Lower Silurian shale using $scCO_2$ as fracturing fluid. They showed that permeability of fractured shale is negatively correlated with effective stress and adsorption-induced swelling. They also indicated that mechanical properties change has a significant influence on the permeability. The total duration of their test was 16 min and the effect of exposure time with $scCO_2$ was not considered. On the other hand, Xiong et al. (2013) showed that poroelastic effects after fluid injection typically result in a temporarily increased aperture followed by aperture decrease in the long term. Recently Zhou et al. (2020) studied the effect of $scCO_2$ saturation time on the fracture permeability of shales. Samples were exposed to $scCO_2$ for a maximum of 24 h and the permeability reduced with the increase of CO_2 saturation time due to adsorption-induced swelling. They also showed that the pressure sensitivity of fracture permeability will change after interaction with $scCO_2$. However, longer exposure times were not considered in their work.

We know that the interaction of $scCO_2$-shale induces physical and chemical alterations in shale, and that has a significant influence on the fluid flow behavior of fractured shales such as gas flow in the process of hydraulic fracturing and $scCO_2$-enhanced shale gas recovery. During the process of $scCO_2$ injection, the gas flow in the fractured shale is primarily controlled by the permeability of shale and hydraulic fracture aperture. Permeability and aperture are affected by various factors including in situ stress, pore pressure, reservoir temperature, adsorption induced swelling, fine particle displacement, CO_2-shale interaction induced mechanical alteration in shale and mineral dissolution (Akono et al., 2019; Gutierrez et al., 2015).

On the other hand, rock fracture roughness has been widely used over the last 40 years because of its important influence on the deformation properties and fluid flow of rock fractures. Various statistical parameters have been suggested in the literature to estimate the joint roughness coefficient (JRC) (Barton, 1973) such as the root mean square roughness height values (RMS), root mean square of the first derivative values (Z_2), average roughness angles (i_{ave}), structure function values (SF), and roughness profile indexes (R_p) (Gao & Wong, 2015; Jang et al., 2014; Tse & Cruden, 1979). Chun and Kim (2001) evaluated these statistical parameters and concluded that joint asperity slope estimates provided by the Z_2 parameter correlate better with JRC values than other parameters.

In this paper, we study the $scCO_2$ saturation time impact, fracture normal displacement and permeability hysteresis as a function of gas pressure, effective stress and fracture surface properties (Z_2 and JRC) in a kinetic process on saw cut and natural fractures of shale samples. We also measured the fracture permeability of samples using argon gas before exposure to $scCO_2$ to study the effect of clay and fine grain displacement on the fracture permeability and fracture displacement. Our results would help one to better understand the chemical-mechanical coupling effect of $scCO_2$-shale interaction on the fluid flow and surface characteristics of a fracture during the hydraulic fracturing and enhanced gas recovery processes.

Table 1
XRD Analysis of the Shale Samples

Sample no.	Fracture type	Depth (ft)	QFP* (%)	Carbonates (%)	Clay + TOC (%)
445P	Natural	12,733.3	17.1	48.1	34.8
7P	Natural	12,551	16.1	71.0	12.9
17P	Saw cut	12,547	20.1	61.2	18.7
469P	Saw cut	12,756	16.7	62.5	20.8

*Quartz + Feldspar + Pyrite.

2. Experimental Setup and Procedures

2.1. Samples

We received samples from the Eagle Ford formation located in South Texas, USA. Eagle Ford shale is located below Austin chalk and above Buda limestone. It is a late Cretaceous-age calcareous formation with a carbonate content of 40%–90% and highly layered with rapidly changing composition with depth, low porosity (2%–8%), total organic content (TOC) ranging from 2%–12%, uniaxial compressive strength of more than 120 MPa and a highly variable matrix permeability measured parallel and normal to the bedding planes (Heller et al., 2014). The cores were collected from a vertical well (i.e., bedding planes normal to the core axis) within the formation based on their proximity to the proposed fields, the presence of core within the relevant reservoir and their availability for sampling. A Rigaku MiniFlex 600 X-ray powder diffraction (XRD) machine was used to determine the mineralogical composition of the core blocks. As shown in Table 1, the composition of the cores varies in terms of clay plus organic matter and carbonate contents.

To prepare the cylindrical samples with a saw cut fracture, we first cored several ~25.4 mm-diameter by 50.8 mm length plugs from the same Eagle Ford shale block. Next, a diamond saw was used to cut the shale plugs at a 30° angle to the long axis of the plug to form a saw cut fracture (Figure 1). The end surfaces of all cylindrical samples were finely polished using ultrafine sandpaper with 16 μm particle size (600 grit) based on the International Society for Rock Mechanics standard. A natural fracture was prepared by coring a cylindrical sample from a selected block with an existing, open and unfilled fracture oriented at almost 90° to the vertical direction (Figure 1c). Two 1.5 mm diameter holes were drilled parallel to the core axis at both ends of each specimen to facilitate fluid flow from the top platen to the fracture plane. To avoid clay mineral-water interactions, samples were cut without using coolant fluids. This technique also prevents oven-drying, which may remove clay-bound water from the samples. To reduce the frictional heating, the saw-cutting was done at low-speed (typically between 100–125 rpm depending on the specimen) and cooled with air blow. It is worth mentioning that the samples were not vacuum-dried to keep the in-situ conditions of the samples and allow the reaction of carbonates and scCO$_2$ in the presence of residual water. Four fracture types with different combinations of shale mineralogy, fracture surface topography and JRC values (Barton, 1973) were prepared: two saw cut fracture samples and two natural fracture samples (see Table 1).

2.2. Experimental Procedure

The permeability measurement experiments were performed using a GCTS triaxial testing system (Figure 2). We jacketed the samples using a 0.75 mm heat-shrink Viton sleeve, which was then sealed on two steel core-holders using flexible steel wires. The confining pressure was measured using a Heise DXD pressure transducer accurate to ±0.1% up to 68.9 MPa. The pore pressure tubes were connected to the sample
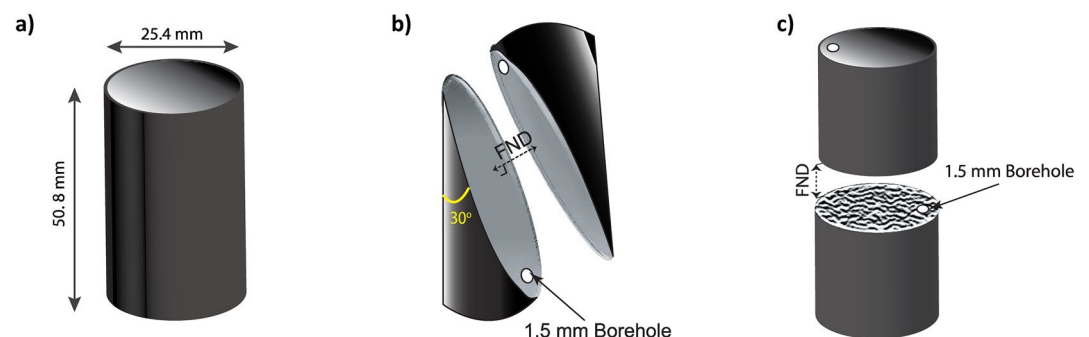

Figure 1. Different sample types and definition of Fracture Normal Displacement (a) cylindrical shale sample (b) saw cut sample (c) Natural fracture sample.
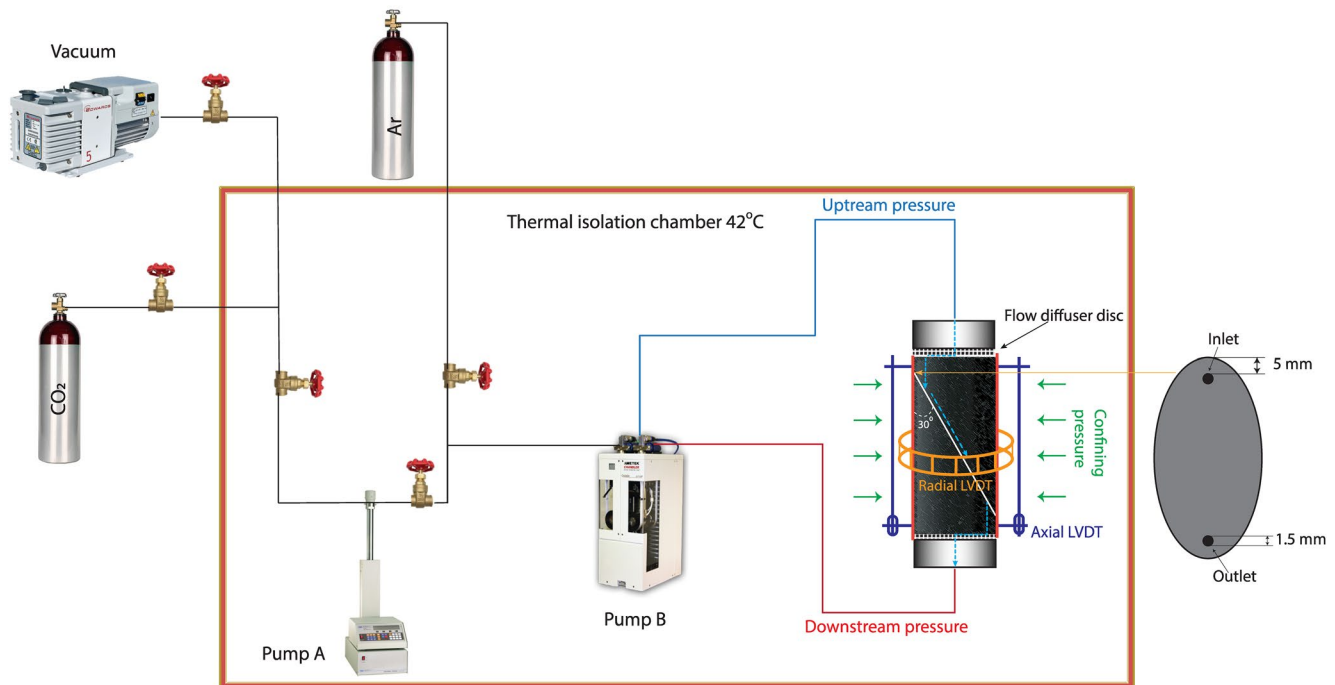
Figure 2. Schematic diagram of the experimental setup (i.e., saw cut sample shown). Isco Pump A is used to boost CO_2 pressure before sending to pump B Quizix Pump B is used to control the upstream and downstream pressures.

through core-holders and the upstream and downstream pore pressures were controlled by the Quizix 6,000 pumps, using two independent cylinders with argon and scCO$_2$ as pore fluids. The pumps, which measure pressures with an accuracy of ±0.3% of the full scale and deliver pressures up to 40 MPa, were used to measure pore pressures and control flow rates. CO_2 state is very susceptible to the temperature change. Thus, four heaters, three thermostats, and a fan were put inside the chamber to thermally insulate inside the chamber and maintain and distribute a constant temperature of 42°C (±0.2°C). An Omega temperature probe was used to monitor the temperature at different locations inside the chamber throughout the experiments.

Silicone oil as the confining fluid and compressed argon gas and then scCO$_2$ were used as the permeating fluid. The permeability measurements were made by either modified pulse-decay or steady-state methods, depending on the sample response to the initial permeability. Using steady-state flow is impractical when it takes a long time to reach the initial equilibrium, and then more time to achieve the steady-state. Thus, we used pulse decay experiment for measuring the permeability in some tests. The details of permeability measurement methods are described in Appendix A.

2.3. Experimental Program

The overall experimental sequence that varied confining pressure and pore fluid pressure as a function of time reported here is shown in Figure 3. A small hydrostatic confining pressure of ~1 MPa was initially applied to the sample accompanied by vacuuming the pore pressure tubes and the sample for 24 h. Then hydrostatic pressure of 5 MPa was applied to minimize stress-relief-induced changes in the microstructure of the sample, followed by application of a confining pressure of 20 MPa for a few hours. Subsequently, a pore pressure of 5 MPa was applied at both upstream and downstream sides using argon, with 12 h for the equilibrium of pore pressures. While keeping the confining pressure at 20 MPa, the pore pressure was elevated to 8 MPa and the argon permeability and fracture displacement measurements were then carried-out at simple effective stresses ($\sigma' = C_P - P_P$, where C_P and P_P are the confining pressure and pore pressure, respectively) of 12 MPa. The pore pressure increased stepwise to 10 MPa, 12 and 14 MPa and the permeability fracture displacement were measured at each step. Then, the pore pressure was lowered to 8 MPa and the mentioned cycle was repeated, and the same measurements were performed at each pore pressure in the
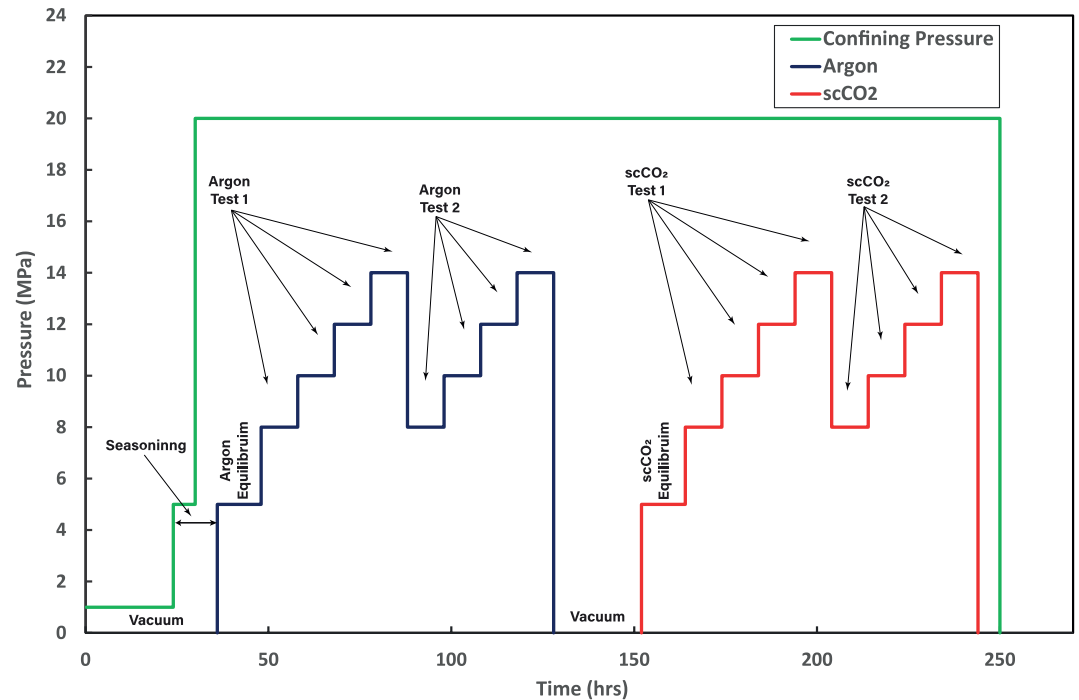
Figure 3. The generic experimental paths for confining pressure, argon and scCO$_2$ followed during the tests.

second cycle. Afterward, the pore pressure was removed, and the sample/tubes were vacuumed for another 24 h to remove any remaining argon. ScCO$_2$ was then introduced into the sample, with an equilibrium/reaction time of 12 h. The same cycle of effective stress as that of argon was applied and eight permeability and fracture displacement measurements were made. The temperature in the chamber was set at ~42°C to make sure that CO$_2$ is kept in the supercritical state during the test. The second cycle was aimed to both assess the permeability hysteresis and the effects of scCO$_2$ over a prolonged period of time on the fracture surface. It should be noted that effective stress magnitudes in this study were considered based on the estimated in-situ stresses with respect to the formation stress regime and depth of the cores.

2.4. Fracture Surface Characteristics

Two vertical and one radial chain LVDT (Linear variable differential transformer) sensors were used to record the vertical and radial displacements of the sample during the test as the fracture aperture evolved. All the LVDT sensors were set to zero just before measuring the permeability in the first argon cycle. The recorded displacement values were used to compute the average displacement normal to the fracture (FND) surface (Figures 1a and 1b). FND values were calculated based on the average vertical and radial displacement of samples measured by LVDTs and the fracture angle using trigonometry. This enabled us to compare the trend of permeability with the actual fracture surface alterations caused by the fluid-fracture surface interactions.

In addition, the surface topographies of the fractures of the four samples were quantitively imaged before and after exposing to argon and scCO$_2$ using a NextEngine 3-D laser scanner with a 2-μm resolution laser beam. We placed the fracture surfaces 20 cm away from the scanner head in a sample holder, which positioned the sample toward the scanner so that the fracture plane was normal to the laser beam and parallel to the scanner. Each fracture surface was imaged at least three times at a resolution of 0.127 mm and the average was used for analysis. The bluish holes on each image show the fluid inlet/outlet boreholes. We took the zero datum at the lowest topographic point near the fluid inlet borehole. While in some images the depth of the borehole was not an issue, in others because of deep boreholes and small topographic changes in the case of the saw cut fractures, we adjust the scale on the color bars for elevation (mm) and thickness (mm) to clearly show topographic features. The thickness of the altered layer (change in topography) for
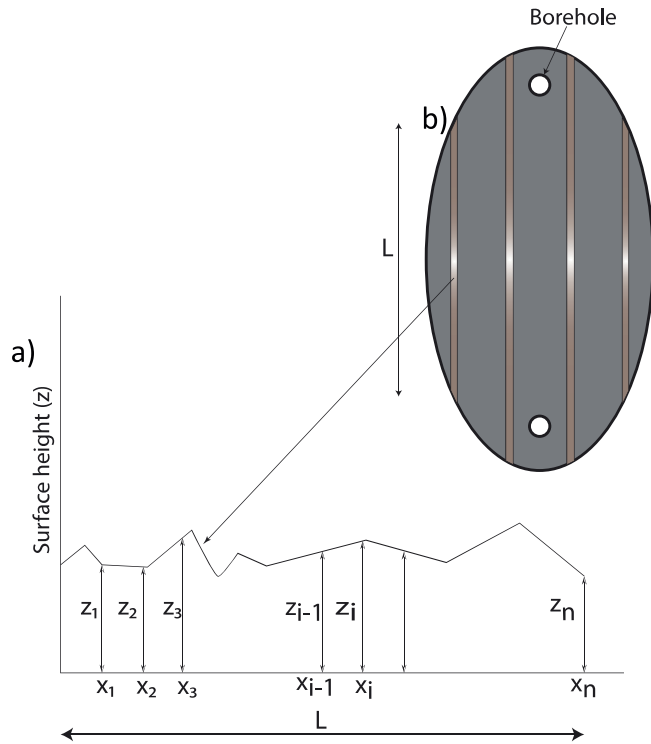
Figure 4. (a) Graph used to define the Z_2 parameter for a joint profile. Here, z_i is the height of a joint profile at x_i, and Δx is the distance between x_{i+1} and x_i. L is the horizontal length of a joint profile (b) Used joint profiles on the fracture to calculate Z_2.

each sample was derived by subtracting the elevation after the permeability experiment from that before the experiment and revealed the size distribution of produced gouge in different fractures.

2.5. Fracture Roughness Parameters

For a single joint profile, Z_2 is given by the following:

$$Z_2 = \left[\frac{1}{L} \sum_{i=1}^{n-1} \frac{\left(z_{i+1} - z_i \right)^2}{x_{i+1} - x_i} \right]^{0.5} \tag{1}$$

where n is the number of data points along the 2-D profile, z_i is the height of a joint profile at x_i and L is the horizontal length of a joint profile. However, Jang et al. (2014) showed that Z_2 is not sufficient for evaluating the JRC, as this parameter is highly dependent on the sampling interval ($\Delta x = x_{i+1} - x_i$). Various sampling intervals such as 0.5, 1 and 2 mm and different types of empirical equations, including logarithmic, linear, square root, and power law, were proposed in previous studies that correlate between Z_2 and JRC values (Jang et al., 2014; Tatone & Grasselli, 2012; Tse & Cruden, 1979; Ye & Ghassemi, 2018). We recorded the fracture surface digitized data in xyz file format to compute the Z_2 parameter after the 3-D scanning using Equation 1. Then, a code was developed in MATLAB to convert the digitized data to surface map topographies. In fact, the 3-D profile of a fracture surface comprised of several 2-D profiles in the flow direction which can be averaged to find Z_2 (Figure 4). We computed Z_2 based on the sampling interval of 0.1 mm for each 2-D profile of the four samples before and after the test and then JRC values of these 2-D profiles were estimated using the power law equation suggested by Jang et al. (2014) as follows:

$$JRC = 54.57 \times Z_2^{0.394} - 19.13 \tag{2}$$

The JRC values computed using the relationships outlined above fall within a $\pm 5\%$ error (i.e., dispersion from the mean value) and range from 0 to 20.

3. Results

3.1. Permeability Evolution of Fractures

The results of permeability measurements of natural fracture and saw cut samples under various effective stresses are illustrated in Figure 5 and listed in tables given in the supporting information. The different stages of the experiment are labeled along the top of each graph. In the plots, the dashed line represents the simple effective stress (effective stress hereafter in this paper) which was changed stepwise from 20 to 6 MPa with four pore pressure steps (P_p = 8, 10, 12, and 14 MPa). The dark blue squares and red circles present the measured fracture permeabilities with argon and scCO$_2$, respectively. Two similar loading/unloading cycles were performed with each fluid to evaluate the permeability evolution with pressure cycling, pore fluid type and possible hysteresis. As expected, the results for all samples show that fracture permeabilities increase as effective stress decreases from 12 to 6 MPa with both argon and scCO$_2$. The permeability of natural fractures (Figures 5a and 5b) are almost two orders of magnitude higher than those of samples with saw cuts (Figures 5c and 5d).

The permeability of sample 445P, a natural fracture with 34.8% of clay + TOC, increased with increasing the pore pressure in the first argon cycle as shown in Figure 5a. In the second cycle, the permeability did not recover, and it increased 40% at $\sigma' = 12$MPa. The highly pressure-dependent and irreversible permeability in the second argon cycle could be attributed to (a) fine-grain displacement and opening the flow channel, (b) high clay and TOC, which are both the most compliant elements of the rock matrix. Upon vacuuming
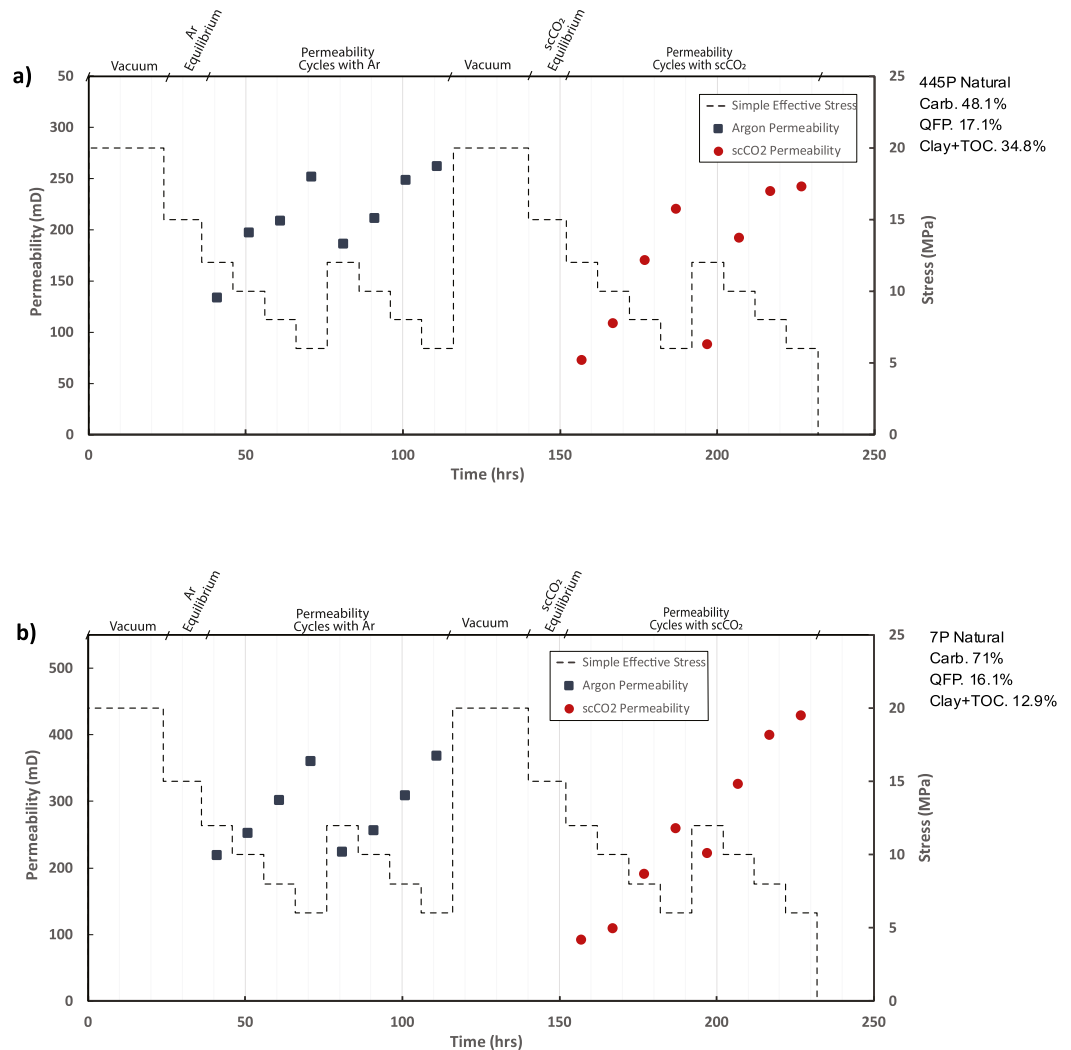
Figure 5. Permeability measurement of (a) sample 445P, a natural fracture (b) sample 7P a natural fracture (c) sample 469P, a saw cut fracture and (d) sample 17P, a saw cut fracture.

the sample and about 24 h of interaction with scCO$_2$, the fracture permeability declined significantly to 73.16 mD exhibiting 61% reduction. This can be attributed to the adsorption of scCO$_2$ into clay minerals and organic matter, which constitute a significant portion of the mineralogical content for this sample (~34.8%). Then permeability increased with decreasing the effective stress. It is well-known that the adsorption-induced swelling could reduce the permeability of fractures in shales depending on the clay types and amount (Akono et al., 2019). Note that this sample has 48.1% carbonates, and hence, some dissolution might have occurred. However, plastic deformation which occurred due to the permanent closure of some of the flow paths resulted from the application of repeated cycles of loading/unloading, and adsorption phenomena are the more dominant factors in this sample. In the second cycle and due to the longer interaction time with scCO$_2$, the permeability increased 10% at $\sigma' = 6$ MPa, which was still lower than argon permeability at the same effective stress. This shows the effect of carbonate dissolution in permeability increase after exposure to scCO2 for more than 3.5 days (~85 h). This argument is further investigated in Section 3.2 where surface topography of the fractures is discussed.

Figure 5b illustrates the permeability values of sample 7P with a natural fracture and carbonate content of 71%. The permeability increased with increasing the pore pressure in the first cycle. Despite a small hysteresis visible during the second argon cycle, the final permeability is nearly identical to the initial value, with less than 2.4% difference suggesting that the flow pathways and cross-sectional areas of the fracture surfaces
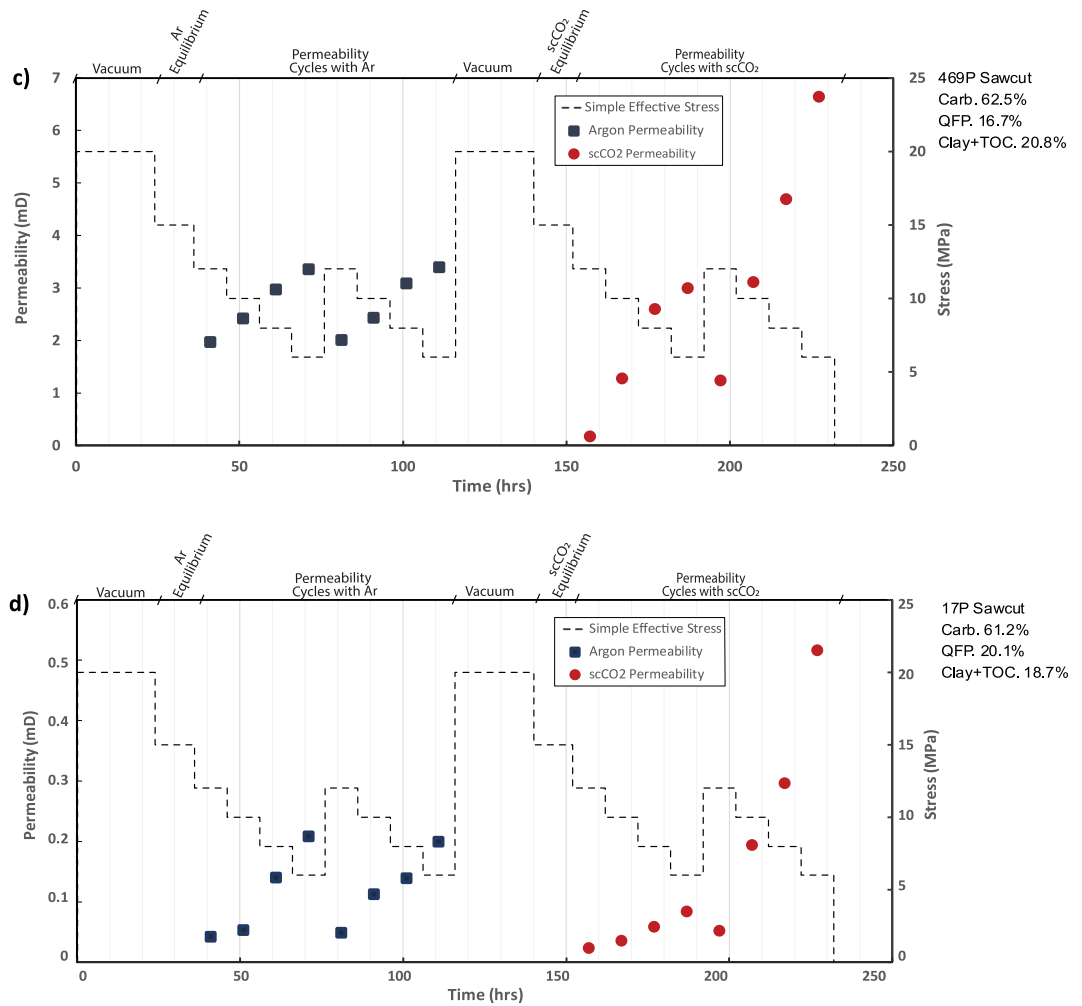
Figure 5. *Continued.*

were stayed intact as no plastic deformation occurred. In the following step, when scCO$_2$ was introduced to the sample, its initial permeability at $\sigma' = 12$ MPa was around half of the argon permeability (i.e., 91.2 mD). This may be due to the adsorption of scCO$_2$ into the clay and organic matter. Upon increasing the effective stress to 12 MPa in the scCO$_2$ second cycle, permeability increased significantly as shown in Figure 5b. This suggests that significant calcite dissolution occurred, and new flow pathways were created on the fracture surface. Reducing effective stress from 12 to 6 MPa and being in contact with scCO$_2$ for more than 3.5 days increased the permeability by 92.8% resulting in the permeability of 428.7 mD.

Sample 469P was a saw cut fracture with 62.5% of carbonates and 20.8% of clay plus TOC. Figure 5c shows the permeability evolution of sample 469P. The permeability increases from 1.96 to 3.35 mD as effective stress decreases from 12 to 6 MPa, exhibiting ~71% increase in permeability, while permeability recovered by 98.5% to a value of 2 mD upon unloading to $\sigma' = 12$ MPa. Upon vacuuming and introducing scCO$_2$ to the sample the permeability decreased dramatically to 0.17 mD at $\sigma' = 12$ MPa. This could be due to the plastic deformation of asperity contacts and compaction of flow pathways caused by vacuuming the sample for 24 h and also CO$_2$ adsorption into the clay and organic minerals. Subsequently, after 3.5 days of exposure to scCO$_2$, carbonate minerals reacted with the carbonic acid, resulting in the dissolution of carbonate minerals, particularly calcite grains. Furthermore, the dissolution of carbonate minerals that reacted with scCO$_2$ can explain the significant increase in permeability of the sample. Permeability elevates to a value of 6.63 mD at $\sigma' = 6$ MPa in the second scCO$_2$ cycle.

Permeability evolution of sample 17P is shown in Figure 5d with an initial permeability of 0.042 mD, which is more than 46 times lower than that of sample 469P. The carbonate content of sample 17P is almost equal to sample 469P and QFP values in sample 17P are 5% higher than that of sample 469P. In the first cycle, by decreasing effective stress from 12 to 6 MPa we observed that the pressure dependency of argon permeability is similar to sample 469P. The permeability increased to 0.28 mD, almost 5 times larger than the initial value. In the second argon cycle, the recovery percentage of permeability is 96% at $\sigma' = 6$ MPa which suggests that the asperity contacts deformed elastically. After vacuuming the sample and then interacting with scCO2 the measured permeability was 50% lower than the previous argon cycle at $\sigma' = 12$ MPa. It should be mentioned that permeability reduction at the same σ' in sample 469P was 91%. This difference is due to the higher QFP and lower clay and TOC contents in 17P compared to 469P. Quartz minerals are expected to undergo only mechanical compaction while mechanical and chemical compaction were observed in carbonates (Zoback & Kohli, 2019). Similar to the sample 469P after longer interaction time with scCO2 in the second cycle, the permeability hysteresis was observed and that increased 522% at $\sigma' = 6$ MPa.

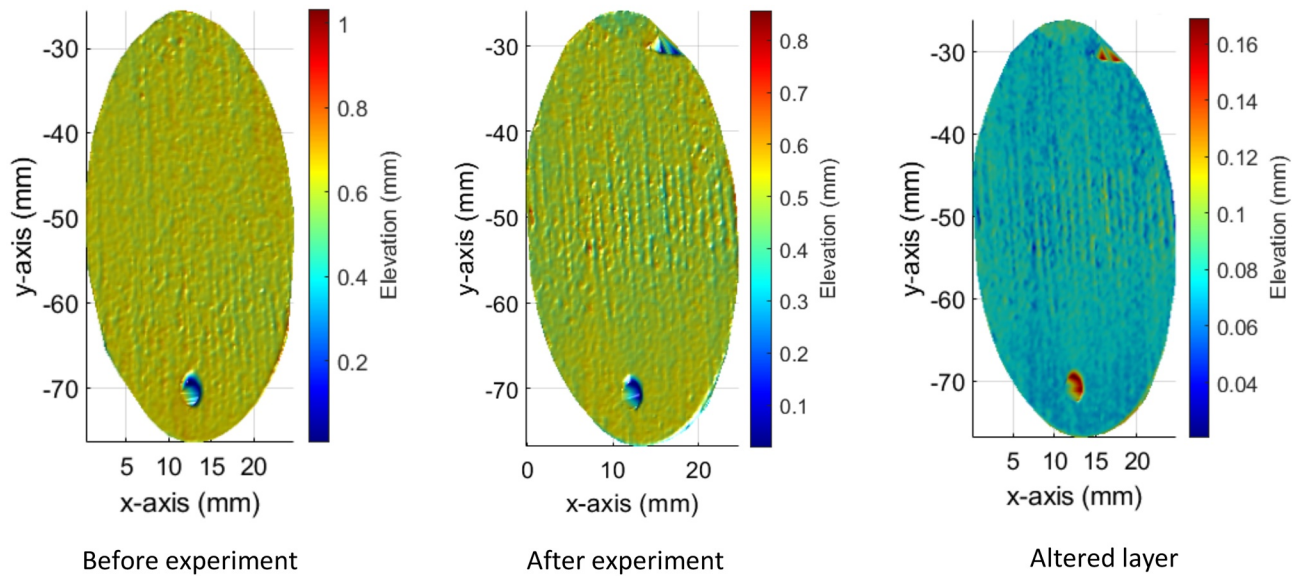### 3.2. Topographic Changes of Fracture Surfaces

The 3-D scanning contours of the surfaces of each fracture are shown in Figures 6 and 7. The topography was mirror-imaged between the corresponding top and bottom fracture surfaces, therefore, a depression on one fracture surface corresponds to a high on the other. Thus, we only showed one fracture surface of each sample. The short axis of the contour in Figures 6 and 7, x, the long axis of the contour 2, y, and the color scale of the contour, z coordinates, of the scanning contours, are the width, length and asperity height of fracture surface, respectively. The color scale in the contour indicates the values of asperity height with respect to the lowest point of the fracture surface (colored dark blue). The dark blue to dark red zones illustrate asperity heights ranging from low to high values. The elliptical and circle contours represent the saw cut and natural fracture samples, respectively. In Figures 6 and 7, the left contour illustrates the fracture surface of the sample before the test and the middle contour indicates the fracture surface of the sample after the test. The right contour shows the altered layer or change in topography due to several loading/unloading cycles and contact with scCO2.

For saw cut fractures, the surface topographies are quite even before the test and some minor corrugations can be observed using high-resolution scan imaging as shown in Figure 6. Both saw cut samples, 469P and 17P, are carbonate-rich samples (61.2% and 62.5% of calcites) and the corrugations were exacerbated on the fracture surfaces after exposing to scCO2 due to calcite dissolution. It should be mentioned that no shear stress applied to samples, and they were under hydrostatic stress condition during the test. Based on the thicknesses of the altered layers in both samples, the maximum asperity elevation changes after argon and scCO2 exposure were calculated. The maximum fracture surface reliefs between the peak point and lowest point of the surfaces are 0.09 and 0.27 mm for samples 469P and 17P, respectively.

For natural fractures, the topography varied considerably across the fracture surface of samples (Figure 7). In sample 445P with high clay and organic matter, the fracture surface swelled after contact with scCO2. The potential expansion of the interlayer clay spacing depends on the initial hydration state of the clay and scCO2 whereby the clay with one water layer of hydration is stable. But two water layers of hydration layer clay loses water when exposed to anhydrous scCO2 (Schaef et al., 2012). Giesting et al. (2012) also reported that montmorillonite can expand up to 9% upon interacting with CO2, with the degree of swelling depending on the initial H2O clay content. This expansion is also reflected in the FND which is discussed in Section 3.3.

The change in topography across the fracture surface of the sample 7P, a natural fracture with high carbonate content, is distributed almost uniformly compared to sample 445P. Asperity degradation is observed on the fracture surface due to carbonate dissolution (Figure 7b). These fracture surface reductions may also result from the removal of the clay coatings on the grains causing the structural integrity of the core to deteriorate. Torsæter and Cerasi (2018) showed that these alterations increase porosity and permeability (about 205%) of the fracture. The thicknesses of the altered layers in both natural fractures were nonuniform similar to the initial fracture surfaces. The highest reduction of asperity elevation after contact with scCO2 is about 0.63 mm in the sample (7P) and the maximum surface expansion in the sample 445P was ≈0.30 mm

a) Sample 469P

Before experiment · After experiment · Altered layer

b) Sample 17P

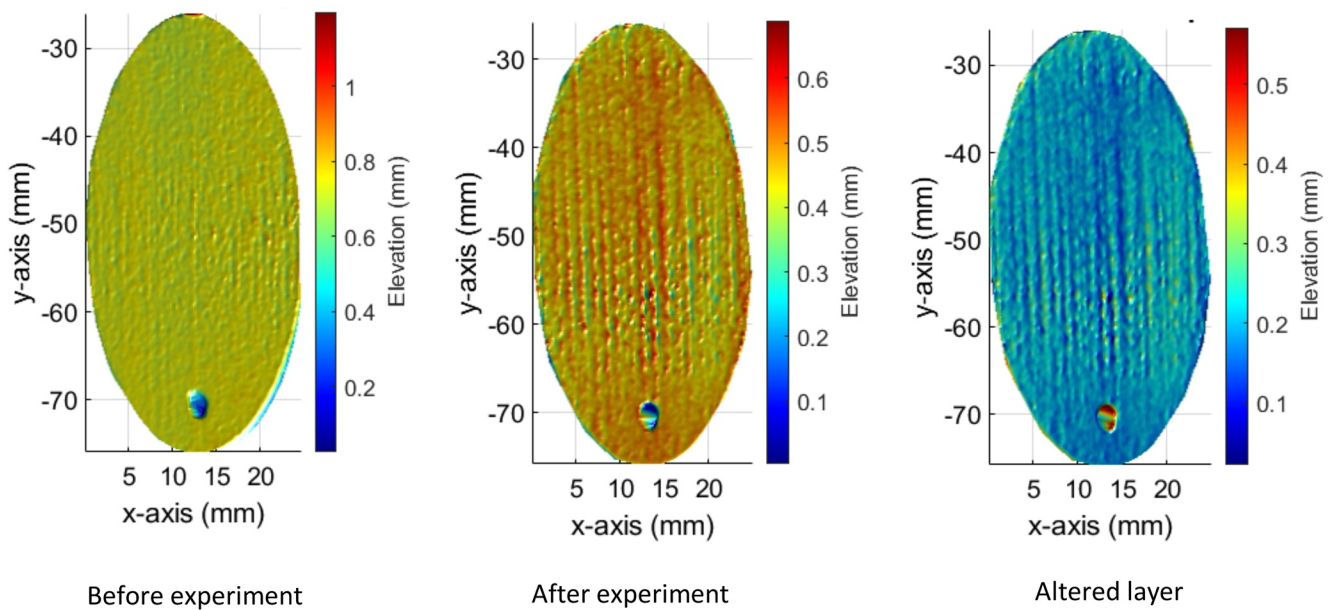Before experiment · After experiment · Altered layer

Figure 6. Surface map topography of saw cut fractures. (a) Sample 469P, (b) sample 17P before (left column) and after (middle column). The right column shows the thickness of the altered layer (change in topography) in each case.

as shown in Figure 7. In a typical shear slip test, the topographic changes happen at peak points where asperities are abraded during slip. However, in our study, most significant topographic changes on the fracture of sample 445P were observed somewhere between the center and periphery of the fracture surface which are shown by dark blue color. While the surface topographic reduction on the surface fracture of 7P sample was almost uniformly distributed on the fracture surface. Thus, the analysis of surface topography provided persuasive evidence to conclude the fact that scCO$_2$-shale interaction resulted in significant surface degradation in fractures with high carbonate content. However, as indicated by Zhou et al. (2019) the degree of
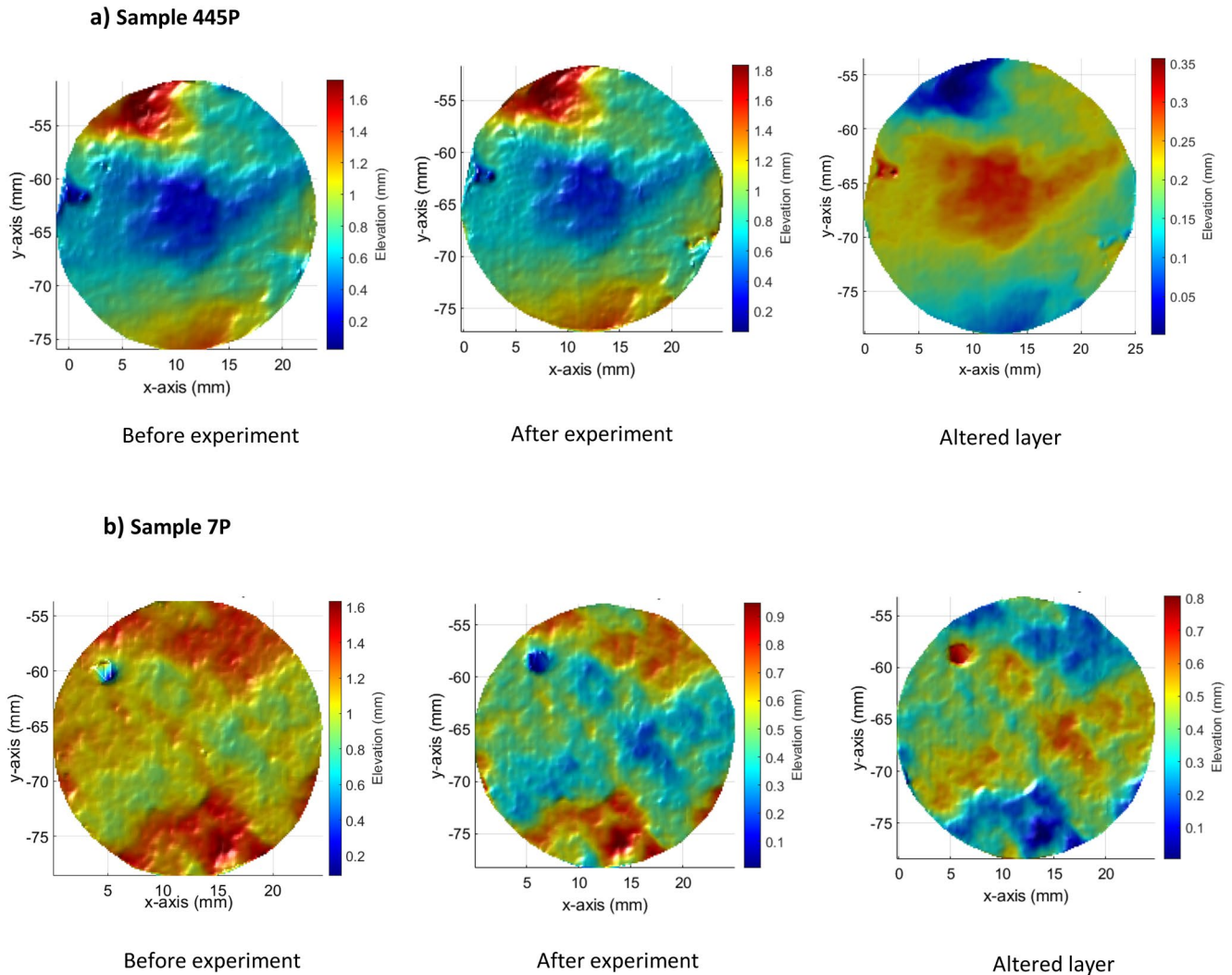
a) Sample 445P

| Before experiment | After experiment | Altered layer |

b) Sample 7P

| Before experiment | After experiment | Altered layer |

Figure 7. Surface map topography of natural fractures. (a) Sample 445P, (b) sample 7P before (left column) and after (middle column). The right column shows the thickness of the altered layer (change in topography) in each case.

mechanical properties change is influenced by multiple factors, including geo-environment characteristics of shale formations, CO_2 phase, adsorption pressure, interaction time, etc.

3.3. Fracture Normal Displacement and Permeability Evolution

Figure 8 shows the changes of the average displacement normal to the fracture (FND), the permeability and the corresponding effective stresses for all four samples. It is well-known that different hydromechanical and chemical processes such as stress changes and mineral dissolution/precipitation triggered by fluid-fracture surface interactions can result in decreasing or increasing the fracture aperture. The processes caused by fluid-fracture interactions alter the aperture, leading to an increase/decrease in the upstream pore pressure to maintain the constant injection rate; consequently, the ΔP increases/decreases accordingly. For instance, as the aperture increases, the upstream pore pressure intensifier lowered the upstream pore pressure (and subsequently, ΔP) to maintain the constant injection rate. Then, the increase in ΔP leads to an increase in the permeability (to maintain the constant flow rate), which in turn leads to an increase in FND. It can be observed in Figure 8 that with changing the effective stress and permeability, the measured FND successfully captures the fracture response. The range of recovery of the permeability and FND upon unloading varies in different samples and are discussed in detail in this section.
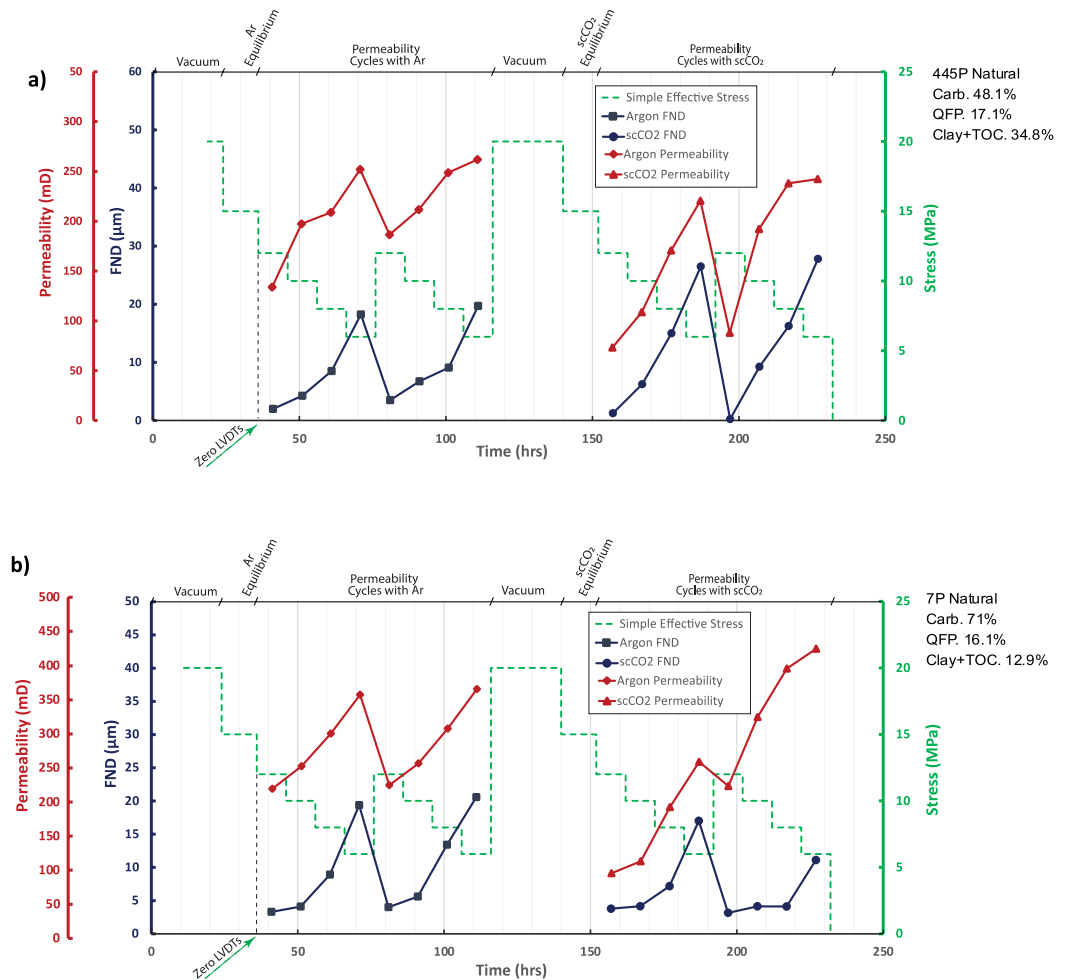
Figure 8. Permeability and Fracture Normal Displacement (FND) measurements of (a) Sample 445P, a natural fracture (b) sample 7P a natural fracture (c) sample 469P, a saw cut fracture and (d) sample 17P, a saw cut fracture.

For sample 445P, a clay-rich natural fracture, both the permeability and FND are pressure-dependent and are in the range of micrometers. In the first argon cycle, the initial FND is 2 μm at $\sigma' = 12$ MPa and that increases to 18.25 μm when the effective stress reduces to 6 MPa. Upon unloading and reloading the sample, the permeability showed higher hysteresis behavior than FND, suggesting that fine-grain migration, which creates a self-propping aperture, has less impact on FND compared to permeability. Afterward, when the sample was vacuumed and scCO$_2$ introduced to the sample the FND reduced to 1.25 μm indicating that the last two cycles of loading and unloading caused plastic compaction on the fracture surface, as that even exacerbated in the second scCO$_2$ cycle.

Sample 7P is a natural fracture with a carbonate content of 71% and the effect of fine particles migration on FND during argon injection is less significant than that of sample 445P. FND increased 21.5% in the second argon cycle at $\sigma' = 12$MPa, while the FND increase was 75% in sample 445P at the same σ'. After vacuuming the sample and introducing scCO$_2$, the fracture FND fully recovered suggesting that the strong carbonate and quartz minerals prevented the fracture surface from plastic compaction, unlike sample 445P. The permeability and measured FND showed pressure dependency in the first scCO$_2$ cycle, and both increased with lowering the effective stress. Due to the longer period being in contact with scCO$_2$, while the permeability increased stepwise with increasing the pore pressure, the rate of FND increase reduced and it even slightly decreased (0.5%) at $\sigma' = 8$ MPa indicating that the carbonates dissolved and new flow pathways were created on the fracture surface. However, further increase of the pore pressure from 12 to 14 MPa ($\sigma' = 6\ MPa$) led to FND increase ($\approx$170%) to enable conducting the flow to downstream.
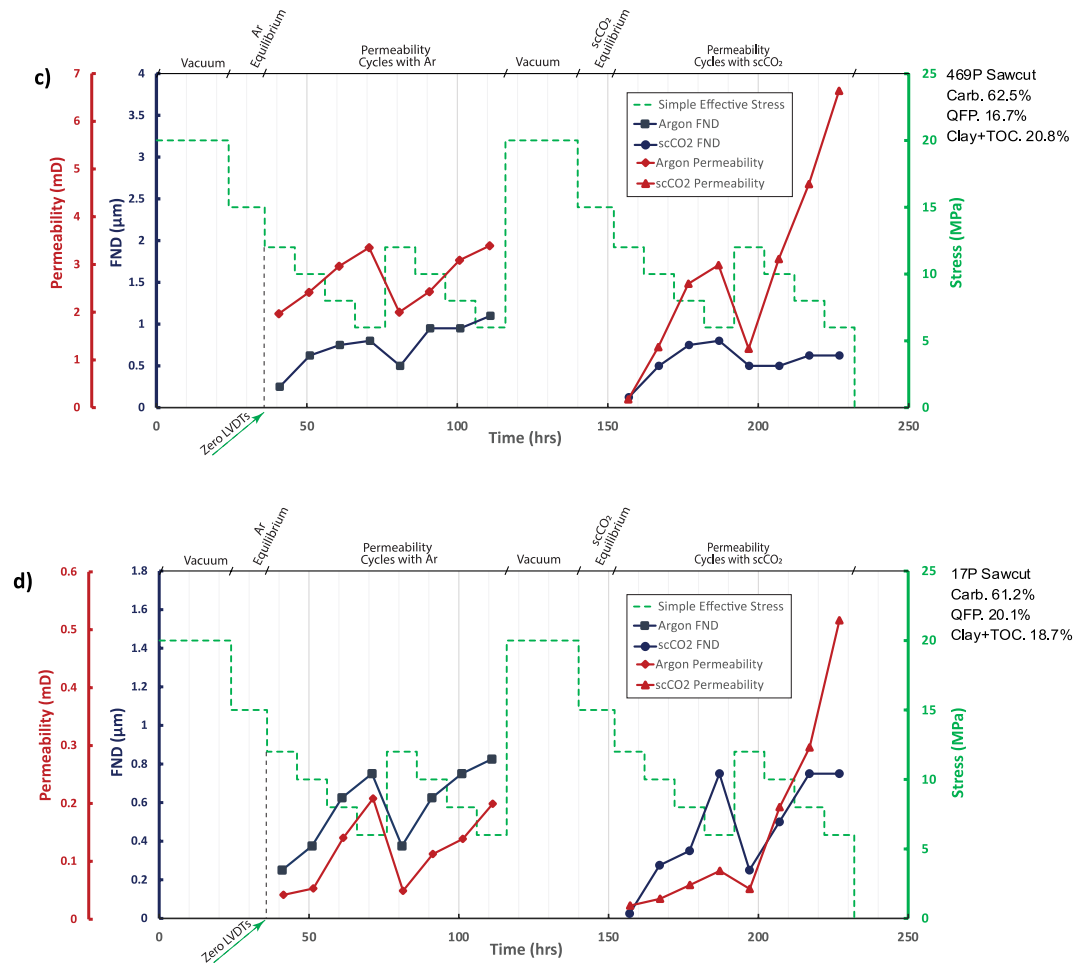
Figure 8. *Continued.*

Figure 8c illustrates that in both argon cycles, the measured FND values correlate well with permeability change in sample 469P. When the sample was vacuumed for 24 h and then exposed to $scCO_2$, the permeability dropped from 1.99 to 0.17 mD (91% reduction) which may be due to $scCO_2$ adsorption into clay minerals on the fracture surface. The FND decreased from 0.5 to $0.125\,\mu m$ at $\sigma' = 12\,\text{MPa}$ due to several loading and unloading cycles which led to plastic deformation. However, at the beginning of the second $scCO_2$ cycle, the permeability and FND both showed hysteresis behavior and did not recover. The permeability increased 122% and FND reduced 21.8% at $\sigma' = 6\,\text{MPa}$ in the second cycle.

For sample 17P, the trend of permeability and FND curves mirrors each other in the first and second argon cycles and a strong correspondence can be observed between the FND and permeability. It can be inferred that the fracture elastically deformed, and the permeability changed only from 0.042 to 0.049 mD in the second cycle. The FND decreased by 90% when the sample was vacuumed and then exposed to $scCO_2$. It shows that the effect of loading/unloading cycles is significant in fracture deformation. The rate of permeability and FND change are 0.002 and 0.024 $\mu m / h$ respectively when σ' decreased from 12 to 6 MPa and the fracture was exposed to the $scCO_2$. This suggests that in order to keep the flow at a certain rate and compensate for the fracture compaction, the actual displacement normal to the fracture surface has to increase 12 times faster than the permeability in the first cycle. Because carbonates did not fully dissolve, and the fracture pathways clogged due to the adsorption of CO_2 into the clay and organic matter particles. In the second cycle, when the sample was in contact with CO_2 for more than 3.5 days (~ 85 h), the FND remained almost unchanged while the permeability increased. This could be attributed to the dissolution of carbonates and creating new flow pathways on the saw cut fracture as was already illustrated in Figure 5b.
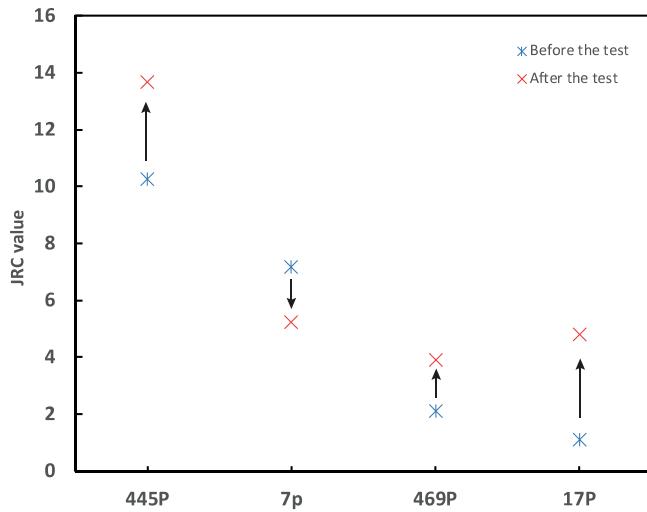
Figure 9. Joint Fracture Coefficient (JRC) values before and after the test.

3.4. Joint Roughness Coefficient

The JRC values for all four samples are illustrated in Figure 9. Increasing JRC from 10.29 to 13.70 in sample 445P, suggests that the fracture surface became rougher when exposed to $scCO_2$. However, the JRC value decreased from 7.20 to 5.24 in sample 7P, after contact with $scCO_2$. Decreasing the JRC value in this natural fracture could be due to intensive carbonate dissolution on the fracture surface. The JRC values of saw cut fractures 469P and 17P increased from 2.12 and 1.13 to 3.92 and 4.83 respectively. New flow pathways were created on the fracture surface because of carbonate dissolution in carbonate-rich samples and the amplitudes of asperities increased on the fracture surface after exposure to $scCO_2$. The results show that for the fracture with high contents of strong minerals including quartz and carbonates the fracture roughness correlates well with initial permeability: a higher JRC value leads to a greater permeability. However, other major processes including adsorption into clays and organic matter and dissolution of carbonates control the final permeabilities as discussed earlier in this section.

4. Discussion

The surface topography analysis of the fractures and measuring the fracture displacement during the experiments helped us to better analyze the permeability evolution in the samples. In Figure 5a, we showed that the permeability of sample 445P, a clay-rich natural fracture, reduced remarkably when the sample was exposed to $scCO_2$ and then increased with increasing the pore pressure. While the adsorption phenomenon and inelastic deformation are expected to result in further reducing the permeability in the subsequent cycle, the permeability increased. The results from topography imaging (Figure 7a) showed that swelling of clay minerals was not distributed uniformly on the fracture surface and that could couple with carbonate dissolution to increase the permeability after 3.5 days ($\sim$85 h).

Sample 7P is a natural fracture with a high carbonate content of 71%. In the second $scCO_2$ cycle we observed that the permeability increased with decreasing the effective stress from 12 to 8 MPa, but the FND stayed almost constant within this range. This suggests that significant carbonate dissolution occurred, and new flow pathways were created on the fracture surface. The asperity degradation on the fracture surface of sample 7P was also clearly observed in topography images as shown in Figure 7b. It is worth mentioning that sample 7P has less clay and organic matter content than sample 445P (12.9% vs. 34.8%) with the relatively same amount of QFP, which together could explain the general lower permeability of 445P sample. In fact, the higher amount of clay and organic matter contributes to the clogging fluid flow pathways.

In the case of saw cut samples, 469P and 17P, a greater pressure dependency in the second $scCO_2$ cycle is an indication that the fracture surface, which creates the fluid flow pathways, was getting more compliant due to interaction with $scCO_2$. This was also shown in surface topography images that new flow pathways were created on the fracture surface when carbonate dissolution occurred. FND did not change in the second cycle in sample 469P remarkably with increasing the pore pressure (Figure 8c), as the $scCO_2$ flow found its way through new flow channels. In sample 17P, it took more time for creating new flow paths and the FND increased until the effective stress of 8 MPa and then stayed constant at $\sigma' = 6$ MPa in the second $scCO_2$ cycle. Higher QFP and lower carbonate contents of 17P could be the reason for the delay in creating new flow paths in this fracture. However, this needs to be further investigated. Thus, carbonate dissolution altered the height, shape, and distribution of asperities on the fracture surface and that could explain the significant increase in permeability in those fractures.

5. Conclusions

Our results showed that carbonate dissolution and inelastic compaction during multiple loading/unloading cycles appear to mitigate each other's impact in controlling permeability. Fracture permeability changes associated with changes of effective stress correlates well with the FND. Apparently, the effect of grain migration in creating a self-propping aperture was more pronounced at the initial stages of the test. As the sample experienced more loading and unloading cycles, the effect of plastic compaction dominated the permeability and FND, especially in the clay-rich fracture.

In the natural fracture sample with high carbonate content, no FND hysteresis was observed when $scCO_2$ was introduced to the fracture and the permeability was overshadowed by adsorption-induced swelling. Then, fracture surface degradation was detected after exposure to $scCO_2$ for more than 3.5 days ($\sim$85 h).

In saw cut fractures the permeability increased (up to 522%) after exposure to $scCO_2$ for more than 3.5 days and 3D scanned images of the fracture surface revealed that the corrugations on the fracture surface were aggravated. The greater pressure dependency of permeability with $scCO_2$ saturation time is an indication that the fracture surface on which the new flow pathways were created, was getting more compliant. That led to FND reduction and mechanical weakening of the fracture surface. Thus, the time-dependency of the carbonate dissolution and framework deterioration process was confirmed in carbonate-rich samples.

The results showed that for the fractures with higher contents of strong minerals including quartz and carbonates the fracture roughness correlates well with permeability: a higher initial JRC value indicates a greater permeability. However, the JRC value does not solely control the final permeability and based on the used approach in this study, we could not establish a direct correspondence between JRC and permeability after the test. We believe other major processes including inelastic deformation, adsorption into clays and organic matter and dissolution of carbonates must be considered as well when evaluating the final permeability.

Appendix A: Fracture Permeability Measurement Methods

To carry out steady-state flow permeability measurements, the desired pore pressure is applied to the sample and left to equilibrate. The experiment can be run by either maintaining a constant pressure differential until inflow equals outflow (and measuring the flow rate) or by imposing constant flow rate conditions and monitoring upstream and downstream pressure until the pressure differential becomes constant. We applied a constant flow rate of 0.1 ml/min and the pressure difference across the sample was measured. As mentioned earlier, each cylinder within the Quizix QX-6000 pump was connected to one end of the core sample inside the triaxial cell. This enabled us to maintain a constant flow rate across the core by setting the upstream and downstream flow rates to +0.1 ml/min and −0.1 ml/min, respectively. Once upstream and downstream pressures were stabilized, we used the modified Darcy's equation for a compressible gas to calculate gas permeability:

$$k_a = -\frac{Q\mu L}{A} \times \frac{2p_d}{p_d^2 - p_u^2} \tag{A1}$$

where k_a is the gas permeability, μ is the gas viscosity, Q is the gas flow rate, L is the length of the sample, A is the cross-sectional area of the sample, p_d is the downstream pressure and p_u is the downstream pressure.

The pulse decay method is known as the most common experimental method to determine permeability in low permeability porous media (Heller et al., 2014). Unlike the steady-state experiments, the gas storage reservoirs of defined volumes are required, on the upstream and downstream ends of the sample. We measure the upstream and downstream pressures by pressure transducers, while the pressure difference between upstream and downstream ends is calculated. The isothermal conditions and well-insulated temperature-controlled system is necessary like steady-state experiments. Since the volumes of the storage reservoirs are identical, as the gas moves through the sample a pressure decrease in the upstream results in a pressure increase in the downstream reservoir and the overall pore volume compressional changes are zero (Pan et al., 2015). To carry out a pulse decay experiment, we subjected the fracture to the desired confining pressure, and gas was injected on both upstream and downstream ends to reach the desired equilibrium

pressure. When the system is equilibrated, a small pressure pulse is applied to the upstream cylinder; however, instead of letting it decay, the upstream pressure is kept constant, thus creating an infinite reservoir (Zoback & Byerlee, 1975). This imposes a pressure change on the upstream end, and gas flows through the sample with a pressure pulse. The downstream pressure increases (and the pressure difference decreases) over time as equilibrium pressure is approached. The constant upstream pressure compensates for any leak on the upstream end of the system (Heller et al., 2014) and any adsorption phenomena (Metwally & Sondergeld, 2011) that may affect permeability measurements. For permeability measurements on samples, we applied a pressure differential of 50 psi in the upstream gas cylinder to reduce changes in gas properties. The rate of decay depends on the permeability and decreases for lower permeabilities. Based on the assumption that storage in a sample is negligible and the pressure gradient across the sample length is nearly constant Brace et al. (1968) showed:

$$\left(p_u - p_f\right) = \Delta p_0 \frac{V_d}{V_u + V_d} e^{-\alpha t} \tag{A2}$$

where p_u is the upstream pressure, p_f is the final equilibrium pressure that upstream and downstream pressure approach; Δp_0 is the initial step change in upstream pressure; V_u and V_d are the volumes of the upstream and downstream gas storage reservoirs (m^3), respectively; t is time, and α is the slope of the decay curve in the semi-logarithmic plot of ($p_u - p_d$) versus time. Thus, the permeability (k) can be calculated as:

$$k = -\frac{\alpha \mu \beta L}{A\left(\dfrac{1}{V_u} + \dfrac{1}{V_d}\right)} \tag{A3}$$

where L is the distance between the two drilled boreholes on the fracture plane, A is the cross-sectional area of the fracture plane and β is the compressibility of the gas (Pa^{-1}). Due to the infinite upstream gas supply, the upstream volume will not be considered in the solution and the Equation A3 will be reduced to:

$$k = -\frac{\alpha \mu \beta L V_d}{A} \tag{A4}$$

For both permeability techniques, the flow pathways between upstream and downstream and the cross-sectional areas of the fractures, which depend on fracture aperture, are unknown. But for given fractures under consistent surface preparation and similar geometry, it was assumed that the fracture surface is planar, flow lines are parallel from the high to low-pressure sides and variation of asperity geometry is insignificant to simplify the evaluation of the fracture permeability. Therefore, relative permeabilities were compared throughout the experiments.

We used modified cubic law with parallel plate approximation (Witherspoon et al., 1980) to estimate the equivalent hydraulic aperture based on the measurements in the steady-state flow regime as follows:

$$b = \left(-\frac{12\mu L Q}{w \Delta P}\right)^{\frac{1}{3}} \tag{A5}$$

where b is the equivalent hydraulic aperture, ΔP is the differential pressure and w is the fracture width. Fracture surfaces are either elliptical or circle and each contains a borehole. The fluid flow zone is assumed as a rectangle/square (Figure A1) with the same area as the ellipse/circle to calculate the fracture permeability. In Figure A1, L is the distance between two boreholes on the fracture surface and the width of the rectangle (w) is calculated by dividing the area of the ellipse by the length L. Then, the cross-sectional area of sample (A) is calculated as follows:
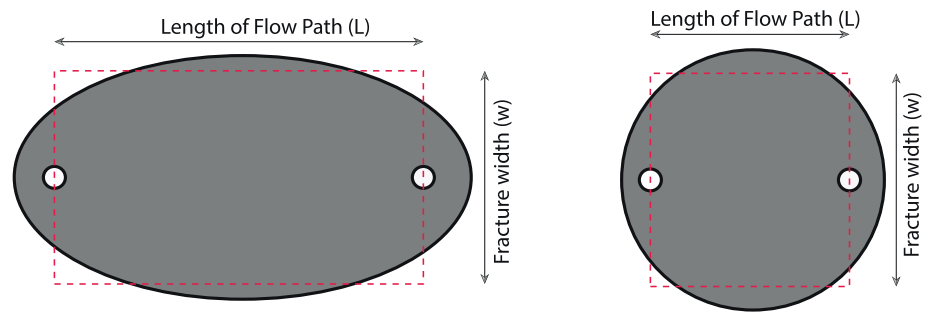
$$A = wb \tag{A6}$$

Figure A1. Fluid flow zone for fracture permeability calculation: The ellipse/circle is the actual fluid flow area, while the rectangular/square area shown by the red dotted lines is the equivalent fluid flow zone.

Data Availability Statement

The measured and calculated data sets for this study are available online (http://dx.doi.org/10.17632/4yrp-ghr5ns.1).

References

Akono, A., Druhan, J. L., Tsotsis, T., Jessen, K., Fuchs, S., Crandall, D., et al. (2019). A review of geochemical–mechanical impacts in geological carbon storage reservoirs. *Greenhouse Gases: Science and Technology*, *504*, 474–504. https://doi.org/10.1002/ghg.1870

Barton, N. (1973). Review of a new shear-strength criterion for rock joints. *Engineering Geology*, *7*(4), 287–332. https://doi.org/10.1016/0013-7952(73)90013-6

Brace, W. F., Walsh, J. B., & Frangos, W. T. (1968). Permeability of granite under high pressure. *Journal of Geophysical Research*, *73*(6), 2225–2236. https://doi.org/10.1029/jb073i006p02225

Chun, B. S., & Kim, D. Y. (2001). A numerical study on the quantification of rock joint roughness. *J KGS*, *17*, 88–97.

Fanchi, J. R. (2005). *Principles of applied reservoir simulation*. Elsevier.

Faoro, I., Elsworth, D., & Candela, T. (2016). Evolution of the transport properties of fractures subject to thermally and mechanically activated mineral alteration and redistribution. *Geofluids*, *16*(3), 396–407. https://doi.org/10.1111/gfl.12157

Gao, Y., & Wong, L. N. Y. (2015). A modified correlation between roughness parameter Z_2 and the JRC. *Rock Mechanics and Rock Engineering*, *48*(1), 387–396. https://doi.org/10.1007/s00603-013-0505-5

Giesting, P., Guggenheim, S., Van Groos, A. F. K., & Busch, A. (2012). Interaction of carbon dioxide with Na-exchanged montmorillonite at pressures to 640 bars: Implications for CO_2 sequestration. *International Journal of Greenhouse Gas Control*, *8*, 73–81. https://doi.org/10.1016/j.ijggc.2012.01.011

Gutierrez, M., Katsuki, D., & Tutuncu, A. (2015). Determination of the continuous stress-dependent permeability, compressibility and poroelasticity of shale. *Marine and Petroleum Geology*, *68*, 614–628. https://doi.org/10.1016/j.marpetgeo.2014.12.002

Heller, R., Vermylen, J., & Zoback, M. (2014). Experimental investigation of matrix permeability of gas shales. *AAPG Bulletin*, *98*(5), 975–995. https://doi.org/10.1306/09231313023

Ishida, T., Aoyagi, K., Niwa, T., Chen, Y., Murata, S., Chen, Q., & Nakayama, Y. (2012). Acoustic emission monitoring of hydraulic fracturing laboratory experiment with supercritical and liquid CO2. *Geophysical Research Letters*, *39*(16). https://doi.org/10.1029/2012gl052788

Jaeger, J. C., Cook, N. G. W., & Zimmerman, R. (2009). *Fundamentals of rock mechanics*. John Wiley & Sons.

Jang, H. S., Kang, S. S., & Jang, B. A. (2014). Determination of joint roughness coefficients using roughness parameters. *Rock Mechanics and Rock Engineering*, *47*(6), 2061–2073. https://doi.org/10.1007/s00603-013-0535-z

Jia, B., Tsau, J., & Barati, R. (2019). Review article A review of the current progress of CO 2 injection EOR and carbon storage in shale oil reservoirs. *Fuel*, *236*(July 2018), 404–427. https://doi.org/10.1016/j.fuel.2018.08.103

Jia, Y., Lu, Y., Elsworth, D., Fang, Y., & Tang, J. (2018). Surface characteristics and permeability enhancement of shale fractures due to water and supercritical carbon dioxide fracturing. *Journal of Petroleum Science and Engineering*, *165*, 284–297. https://doi.org/10.1016/j.petrol.2018.02.018

Kamali, A., Zoback, M. D., & Kohli, A. H. (2021). *Effects of supercritical CO2 on matrix permeability of unconventional formations*.

Li, X., Feng, Z., Han, G., Elsworth, D., Marone, C., Saffer, D., & Cheon, D.-S. (2016). Breakdown pressure and fracture surface morphology of hydraulic fracturing in shale with H_2O, CO_2 and N_2. *Geomechanics and Geophysics for Geo-Energy and Geo-Resources*, *2*(2), 63–76. https://doi.org/10.1007/s40948-016-0022-6

Li, X., & Kang, Y. (2018). Enhanced shale gas recovery using supercritical carbon dioxide. *Science*, 1893–2018.

Lu, Y., Chen, X., Tang, J., Li, H., Zhou, L., Han, S., et al. (2019). Relationship between pore structure and mechanical properties of shale on supercritical carbon dioxide saturation. *Energy*, *172*, 270–285. https://doi.org/10.1016/j.energy.2019.01.063

Maneth Wanniarachchi, W. A., Gamage, R. P., Perera, M. S. A., Rathnaweera, T. D., Gao, M., & Padmanabhan, E. (2017). Investigation of depth and injection pressure effects on breakdown pressure and fracture permeability of shale reservoirs: An experimental study. *Applied Sciences (Switzerland)*, *7*(7), 664. https://doi.org/10.3390/app7070664

Metwally, Y. M., & Sondergeld, C. H. (2011). Measuring low permeabilities of gas-sands and shales using a pressure transmission technique. *International Journal of Rock Mechanics and Mining Sciences*, *48*(7), 1135–1144. https://doi.org/10.1016/j.ijrmms.2011.08.004

Middleton, R. S., Carey, J. W., Currier, R. P., Hyman, J. D., Kang, Q., Karra, S., et al. (2015). Shale gas and non-aqueous fracturing fluids: Opportunities and challenges for supercritical CO_2. *Applied Energy*, *147*, 500–509. https://doi.org/10.1016/j.apenergy.2015.03.023

Pan, Z., Ma, Y., Connell, L. D., Down, D. I., & Camilleri, M. (2015). Measuring anisotropic permeability using a cubic shale sample in a triaxial cell. *Journal of Natural Gas Science and Engineering*, *26*, 336–344. https://doi.org/10.1016/j.jngse.2015.05.036

Pei, P., Ling, K., He, J., & Liu, Z. (2015). Shale gas reservoir treatment by a CO_2-based technology. *Journal of Natural Gas Science and Engineering*, *26*, 1595–1606. https://doi.org/10.1016/j.jngse.2015.03.026

Reinsalu, E., & Aarna, I. (2015). About technical terms of oil shale and shale oil. *Oil Shale*, *32*(4), 291–293. https://doi.org/10.3176/oil.2015.4.01

Schaef, H. T., Ilton, E. S., Qafoku, O., Martin, P. F., Felmy, A. R., & Rosso, K. M. (2012). In situ XRD study of Ca^{2+} saturated montmorillonite (STX-1) exposed to anhydrous and wet supercritical carbon dioxide. *International Journal of Greenhouse Gas Control*, *6*, 220–229. https://doi.org/10.1016/j.ijggc.2011.11.001

Tatone, B. S. A., & Grasselli, G. (2012). Quantitative measurements of fracture aperture and directional roughness from rock cores. *Rock Mechanics and Rock Engineering*, *45*(4), 619–629. https://doi.org/10.1007/s00603-011-0219-5

Torsæter, M., & Cerasi, P. (2018). Geological and geomechanical factors impacting loss of near-well permeability during CO_2 injection. *International Journal of Greenhouse Gas Control*, *76*, 193–199. https://doi.org/10.1016/j.ijggc.2018.07.006

Tse, R., & Cruden, D. M. (1979). Estimating joint roughness coefficients. *International Journal of Rock Mechanics and Mining Sciences*, *16*(5), 303–307. https://doi.org/10.1016/0148-9062(79)90241-9

Witherspoon, P. A., Wang, J. S. Y., Iwai, K., & Gale, J. E. (1980). Validity of cubic law for fluid flow in a deformable rock fracture. *Water Resources Research*, *16*(6), 1016–1024. https://doi.org/10.1029/wr016i006p01016

Xiong, Y., Hu, L., & Wu, Y.-S. (2013). Coupled geomechanical and reactive geochemical simulations for fluid and heat flow in enhanced geothermal reservoirs. In *Proceedings, thirty-eighth workshop on geothermal reservoir engineering*. Stanford University.

Yasuhara, H., Kinoshita, N., Ohfuji, H., Lee, D. S., Nakashima, S., & Kishida, K. (2011). Temporal alteration of fracture permeability in granite under hydrothermal conditions and its interpretation by coupled chemo-mechanical model. *Applied Geochemistry*, *26*(12), 2074–2088. https://doi.org/10.1016/j.apgeochem.2011.07.005

Ye, Z., & Ghassemi, A. (2018). Injection-induced shear slip and permeability enhancement in granite fractures. *Journal of Geophysical Research: Solid Earth*, *123*(10), 9009–9032. https://doi.org/10.1029/2018JB016045

Zhang, X., Lu, Y., Tang, J., Zhou, Z., & Liao, Y. (2017). Experimental study on fracture initiation and propagation in shale using supercritical carbon dioxide fracturing. *Fuel*, *190*, 370–378. https://doi.org/10.1016/j.fuel.2016.10.120

Zhou, J., Hu, N., Xian, X., Zhou, L., Tang, J., Kang, Y., & Wang, H. (2019). Supercritical CO_2 fracking for enhanced shale gas recovery and CO_2 sequestration: Results, status and future challenges. *Advances in Geo-Energy Research*, *3*(2), 207–224. https://doi.org/10.26804/ager.2019.02.10

Zhou, J., Tian, S., Zhou, L., Xian, X., Yang, K., Jiang, Y., et al. (2020). Experimental investigation on the influence of sub- and super-critical CO_2 saturation time on the permeability of fractured shale. *Energy*, *191*, 116574. https://doi.org/10.1016/j.energy.2019.116574

Zoback, M. D., & Byerlee, J. D. (1975). The effect of microcrack dilatancy on the permeability of westerly granite. *Journal of Geophysical Research*, *80*(5), 752–755. https://doi.org/10.1029/jb080i005p00752

Zoback, M. D., & Kohli, A. H. (2019). *Unconventional reservoir geomechanics*. Cambridge University Press.